This article has been accepted for publication in IEEE/ASME Transactions on Mechatronics. This is the author's version which has not been fully edited and content may change prior to final publication. Citation information: DOI 10.1109/TMECH.2026.3662305

Optimization of an Axial Flux Motor-Cycloid Gear Actuator for Sizing Wearable Robots

Myles Cooper, Santiago Canete, Digby Chappell, Conor Walsh

***Abstract*—Actuators for wearable robots are difficult to design due to the competing requirements of minimizing weight and form factor while achieving desired performance requirements. Current solutions often rely on a 'one-size-fits-all' approach utilizing classical motors and gears. Here we present a thin, high torque density wearable actuator consisting of a cycloid gear and PCB axial flux motor, along with a modeling and design optimization framework to minimize actuator and battery mass while maintaining target performance. The model predicts motor mass with 95.9% accuracy and battery power with 75.9-87.9% accuracy. We then apply this design and optimization framework to quantify the benefits of creating optimized sizes of wearable actuators for gait assistance for stroke survivors, which was found to reduce average actuator and battery mass by 384 g with just 5 sizes. Furthermore, sizing the actuator and battery together resulted in an average of 28.9% to 48.3% more weight savings than sizing only the motor or only the battery, respectively, for individually optimized actuators. This paradigm of sizing actuators like clothing, along with new actuator architectures, may yield weight savings that could improve adoption of daily-wear assistive devices.**

***Index Terms*—Design Methodology for Mechatronics, Actuator Design, Design and Human Factors, Prosthetics and Exoskeletons**

I. INTRODUCTION

When designing a wearable robot, minimizing weight and thickness is critical. If the device is perceived as too heavy or bulky, the wearer will likely stop using it [1]. Added distal mass significantly increases the joint torques and powers required to walk [2], and added thickness may interfere with the wearer's natural movements [3] while increasing visual stigma [1], [4]. However, these physical constraints must be balanced against the necessity of achieving a desired assistive power, which typically increases the size and weight of the actuator and battery. Thus, developing methods that balance these objectives could lead to wider community adoption.

In actuator design, balancing the competing demands for performance, weight, and size is difficult. To overcome this, a common strategy in wearable robotics is to use a small-diameter brushless direct-current (BLDC) motor with a high gear ratio transmission [5], [6]. This approach allows for a thin and lightweight actuator package but results in low transmission efficiency and peak acceleration, consequently requiring larger battery sizes and limiting controllability. For this reason, quasi-direct drive (QDD) actuators have gained popularity in wearable robotics [7], [8]. Using axially thin, large-diameter motors paired with a low gear ratio ($\sim$10:1) overcomes efficiency and acceleration limitations but ultimately results in heavier and larger motors [9]. Although both approaches have shown promise, exploring new motor topologies could lead to actuators that preserve performance in a smaller and lighter package.

Axial flux motor topologies are compelling for use in wearable robots due to their high torque density and thin form factor, yet they remain underutilized. By orienting the air gap axially, these topologies achieve superior torque-to-weight ratios in flat geometries, specifically when the diameter-to-length ratio exceeds $\sim$4:1, making them ideal for the slim profiles required in exoskeletons [10], [11]. Some designs have been proposed to assist the upper [12], [13] and lower limbs [14], demonstrating that axial-flux topologies can satisfy torque density and size requirements for wearable robots. Despite the promise, practical adoption is often hindered by complex manufacturing and high tooling costs. Printed circuit board (PCB) stator technology addresses these barriers by eliminating the need for specialized tooling, enabling the economical production of custom lightweight coreless motors. When paired with a thin transmission [11], PCB-based axial flux motors present a promising pathway for accessible, high-performance wearable robotic actuators.

Complementing thin motor topology, cycloid gears are particularly appealing for thickness-constrained applications. By utilizing a single-stage eccentric mechanism to achieve reduction ratios of 10:1 to 100:1, they offer a thinner profile than compound planetary, Wolfrom, or harmonic drives, the latter requiring a bulky flexural element [15], [16]. Although historically uncommon in small-scale robotic applications due to the extreme machining tolerances required to minimize backlash and torque ripple [17], recent precision manufacturing advances have renewed interest in cycloids due to their high efficiency and compactness [15], [16].

With an actuator topology defined, the design must be optimized to minimize actuator mass while meeting specific torque, velocity, and acceleration trajectories for wearable

---

This work was supported by the Eunice Kennedy Shriver National Institute Of Child Health & Human Development of the National Institutes of Health Award BRG-R01HD088619. The content is solely the responsibility of the authors and does not necessarily represent the official views of the National Institutes of Health. This work was also supported by the Massachusetts Technology Collaborative, Collaborative Research and Development Matching Grant. *(Corresponding author: Conor Walsh)*

The authors are with the Harvard John A. Paulson School of Engineering and Applied Sciences, Boston, MA, 02134 USA (e-mail: walsh@seas.harvard.edu)

This work involved human subjects in its research. Approval of all ethical and experimental procedures and protocols was granted by Harvard Medical School Institutional Review Board.

This article has been accepted for publication in IEEE/ASME Transactions on Mechatronics. This is the author's version which has not been fully edited and content may change prior to final publication. Citation information: DOI 10.1109/TMECH.2026.3662305

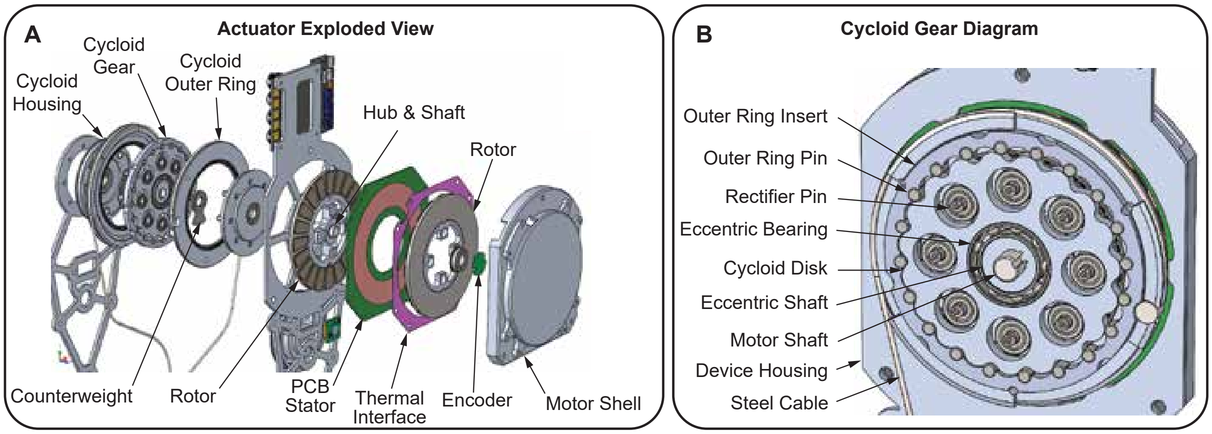

Fig. 1. A: Exploded view of cycloid gear and axial flux actuator integrated into a wearable robot frame. The motor shaft drives the gear input torque while the outer ring rotates to transmit power. B: Diagram of major functional cycloid components.

applications [18]. Unlike previous frameworks that rely on discrete catalogs of commercial components [18]–[20], the scarcity of off-the-shelf axial flux motors and cycloid gears means that fundamental design equations must be used. Defining target trajectories is also complicated by inter-subject variability, such as the heterogeneous gait patterns found in post-stroke gait [21]. To avoid the logistical burden of individual-specific customization, we propose generating sets of actuator sizes tailored to specific population segments. Through an optimization-based framework, actuator geometries can be generated that adequately balance competing performance, weight, and size demands.

In this paper, we present an optimization-based design framework for a wearable robotic actuator consisting of an axial flux PCB motor and cycloid gear. We first describe the overall actuator design, and model the parameters that impact performance, geometry, and weight. We then validate our model using both experimental characterization and comparison to motor datasheets. Finally, we present a case study applying the design framework to the design of a powered ankle exoskeleton. In this case study, we detail how the actuator can be sized and weight can be minimized while achieving specific biomechanics-driven performance requirements.

II. DESIGN FRAMEWORK

In this section, we detail the high-level design and modeling of the actuator. Our primary objective is to design a thin, portable actuator with minimal system weight that can track a desired torque, speed, and acceleration trajectory. We assume that the weight of the cycloid gear, structural components, and electronics are constant and thus the primary drivers of system mass are the motor and the battery. We present models for motor mass, battery mass, and maximum motor torque to provide the foundation for optimizing motor geometry for a given performance requirement.

Design requirements were based on a target use case of assisting the ankle during walking for individuals post-stroke. Based on ankle exoskeleton literature [22], [23] we designed the actuator to apply a peak torque of up to 45 N·m and have a target thickness of ∼30 mm. The actuator is also designed to be modular in both gear ratio and motor geometry, making it adaptable to a range of needs.

A. Cycloid Gear

Cycloid gears are composed of an eccentric input shaft, a cycloid disk, an outer ring, and rectifier pins that constrain the movement of the cycloid disk (Fig.1 B). In a typical cycloid gear, the outer ring is fixed to a housing, and the rectifier pins are attached to an output shaft. In this actuator, the rectifier pins were instead fixed to the housing, allowing the outer ring to act as the output. The outer ring has a diameter of 89 mm and transmits load through two 1.5 mm diameter steel cables that wrap around its outer surface (Fig.1 B). This decreases actuator thickness relative to using rectifier pins, as it removes the need for protruding components from the side of the gear.

The inner rolling components of the cycloid gear were designed to balance mass, size, and efficiency. Ball bearings were used for the rectifier pins and between the input eccentric and the cycloid disk to maximize efficiency. The outer ring uses externally-housed 4 mm diameter AISI 52100 steel rollers as the 'ring pins' that mesh with the cycloid gear. Using externally housed rollers is not as efficient as ball bearings [16], but allows the gear to be significantly more compact.

The eccentric shaft, cycloid disk, and an outer ring insert were designed as 2D cut parts that can be easily changed, allowing the gear ratio to be changed without rebuilding the whole gearbox. The minimum thickness of these components is driven by the maximum contact stress between the ring pins and the cycloid disk, which was calculated to be 4 mm using equations from [24]. Maximum contact stress was found to vary only ∼10% between gear ratios of 10:1 and 100:1, and thus the thickness of these components was treated as constant. We also set the gear eccentricity at 80% of the maximum for a given gear ratio to approximately minimize contact stress, based on a previous analysis [24]. Two steel counterweights are mounted on either side of the cycloid disk to minimize vibration from the eccentric movement of the cycloid disk.

The eccentric shaft is fitted onto the shaft of the axial flux PCB motor, which produces the input torque for the gear.

B. Axial Flux Motor

The motor module of the actuator consists of the PCB stator, two rotors, the rotor shaft, a commutation encoder, and an aluminum shell (Fig.1 A). The stator PCB (ECM PCB Stator, USA) mounts to the aluminum motor cover through a thin thermal interface material (0.003" Tgard K52, Laird, UK). The aluminum cover acts as a heat sink as well as a bearing mount to precisely locate the axis of rotation of the rotor relative to the stator. The rotor shaft has an embedded magnet which is read by an absolute magnetic encoder (AS5047P, ams OSRAM, Austria), which provides position feedback to the BLDC motor driver (ODrive Pro, ODrive Robotics, USA).

Each rotor consists of wedge-shaped neodymium magnets epoxied to two mild steel annular-shaped 'back iron' plates. These plates are pressed on to a two-part aluminum hub that connects the rotors to the rotor shaft (Fig.1 A).

The dimensions of the motor and the gear ratio of the cycloid gear are determined by solving the optimization problem presented in Section IV-B.

C. Modeling

In this section, we present models for motor and battery masses, m_{motor} and m_{batt}, and for the maximum peak motor torque τ_{max}. Models are expressed in terms of gear ratio G_r, motor geometry (R_o, k_d, r_m, t_m, t_s; shown in Fig. 2), and desired actuator performance (τ_{act}, ω_{act}, α_{act}).

1) Motor mass: The motor mass can be approximated as the combined mass $m_{motor} = m_{active} + m_{end}$ of the magnetically-active area m_{active} and the end turn area in the stator m_{end}. m_{active} can be approximated as five annuli: two rotor back-iron m_{bi}, two sets of magnets m_{mag}, and one stator m_{stator}. These annuli are of equal active area $a_{active} = \pi R_o^2(1 - k_d)^2$, where R_o is the active area outer radius and k_d is the ratio of inner-to-outer radius. Thus m_{active} can be computed from the back-iron, magnet, and stator densities (ρ_{bi}, ρ_m, and ρ_s) and thicknesses (t_{bi}, t_m, and t_s):

$$m_{active} = a_{active}(2\rho_{bi}t_{bi} + 2\rho_m t_m + \rho_s t_s). \tag{1}$$

ρ_{bi} is iron alloy dependent and assumed constant. The magnet density is calculated by $\rho_m = r_m \rho_{magnet}$ where r_m is the fraction of the area taken up by magnet material of density ρ_{magnet}. The effective stator density ρ_s is calculated as $\rho_s = r_{cu}\rho_{cu} + (1 - r_{cu})\rho_{fg}$, where r_{cu} is the fraction of the stator area taken up by copper of density ρ_{cu}, and ρ_{fg} is the density of the fiberglass insulation. r_{cu} depends on the packing factor of copper within each slot k_p and the ratio of slot area $a_{slot} = 2\pi R_o^2 k_d(1 - k_d)$ to active area a_{active}:

$$r_{cu} = k_p \frac{a_{slot}}{a_{active}}. \tag{2}$$

End turn mass is calculated as $m_{end} = k_p t_s a_{end}$ where a_{end} is the end turn area, approximated by:

$$a_{end} = \pi \left(\frac{\tau_{si}}{2}\right)^2 + (\tau_{so} - \tau_{si})\frac{\tau_{si}}{2}, \tag{3}$$

where $\tau_{si} = R_o k_d 2\pi/N_s$ and $\tau_{so} = R_o 2\pi/N_s$ are the slot pitch at the inner and outer radii, respectively, and N_s is the number of stator poles. We assume $N_s = 0.75N_p$ where N_p is the number of magnets per stator half, according to the stator PCB manufacturing options available (ECM PCB Stator; MA, USA). This assumption also allows us to define a constant winding factor $k_w = 0.866$ [25]. N_p must be a multiple of four for this assumption to be valid, but we model the magnet and stator poles as continuous variables for ease of optimization.

To create a low-reluctance flux linkage between magnets, the rotor back-iron must have sufficient thickness t_{bi} to keep the average flux density below the steel's saturation flux density. To approximate the minimum sufficient back-iron thickness, we adapt equation 6.56 from [26]:

$$t_{bi} = \frac{B_g}{2B_{bi}}\frac{2\pi R_o}{N_p}, \tag{4}$$

where B_g is the mean air gap flux density and B_{bi} is the maximum allowable back iron flux density. B_g can be expressed as a function of motor geometry $B_g = f(R_o, k_d, r_m, t_m, t_s, g)$, where g is the air gap thickness, from equation 4.13 from [26].

Since t_{bi} is inversely proportional to N_p, we assume that the optimal number of poles is the maximum number allowable, limited by either the maximum electrical frequency of the chosen BLDC motor driver $\omega_{elecMax}$ or by a manufacturing-determined upper limit N_{pMax}:

$$N_p = \min\left(N_{pMax},\ 2\frac{\omega_{elecMax}}{\max(\omega_{act}G_r)}\right), \tag{5}$$

where ω_{act} is the actuator's velocity and G_r is its gear ratio.

2) Battery mass: To approximate battery mass, we assume that the battery must have sufficient capacity to fulfill maximum discharge rate, RMS discharge rate, and device run time.

A lithium battery's rated discharge current can be expressed as the multiple of the battery's capacity that can be discharged in one hour, C. Discharge rate is limited by a peak 'burst' discharge rate C_{max} as well as a continuous discharge rate C_{cont}. The continuous discharge rate is a thermal limitation based on the ohmic losses within the battery and can be approximated using the RMS current for a transient trajectory.

Assuming constant battery voltage, C values can be used to determine the required energy capacity E of the battery:

$$E_{max} = \frac{\max(P_{batt})}{C_{max}}, \tag{6}$$

$$E_{cont} = \frac{\text{RMS}(P_{batt})}{C_{cont}}, \tag{7}$$

where P_{batt} is the electrical power drawn by the battery. If device run time t_{run} is the limiting factor, the required battery capacity can be approximated using the mean battery power:

$$E_{run} = \text{mean}(P_{batt})t_{run}. \tag{8}$$

The maximum value of these three potential energy capacities can then be used to calculate battery mass using the energy density of the battery chemistry ρ_{batt}:

$$m_{batt} = \frac{1}{\rho_{batt}}\max\left(E_{max}, E_{cont}, E_{run}\right). \tag{9}$$

The total battery power is calculated as

$$P_{batt} = P_{mech} + P_{loss} \tag{10}$$

This article has been accepted for publication in IEEE/ASME Transactions on Mechatronics. This is the author's version which has not been fully edited and
content may change prior to final publication. Citation information: DOI 10.1109/TMECH.2026.3662305

where P_{loss} is the sum of all electrical losses, and P_{mech} is the mechanical power produced by the motor, defined as:

$$P_{mech} = G_r \tau_{motor} \omega_{act}. \tag{11}$$

τ_{motor} is the required motor torque, modeled as per [27]:

$$\tau_{motor} = \frac{\tau_{act}}{\eta^{\mathrm{sgn}(\tau_{act}\omega_{act})} G_r} + J\alpha_{act} G_r, \tag{12}$$

where η is the cycloid gear efficiency, τ_{act} is the actuator load torque, α_{act} is the actuator acceleration, and J is the total rotor moment of inertia. We model $\eta = f(G_r, \eta_0)$ as in [15]:

$$\eta = \frac{\eta_0}{G_r(1 - \eta_0) + 1}, \tag{13}$$

where η_0 is bearing efficiency, assumed to be constant based on the cycloid gear construction. J can be calculated by:

$$J = 2a_{active}(\rho_{bi} t_{bi} + \rho_m t_m) R_o^2 (1 - k_d^2). \tag{14}$$

To model P_{loss}, as in many robotics applications, we assume that torque-dependent losses will dominate speed-dependent losses [28]. We further assume that resistive losses in the stator windings P_r will be the dominant source of power loss, and can be approximated by $P_r = \tau_{motor}^2 / k_m^2$ where k_m is the 'motor constant'. To account for other torque losses, such as losses due to temperature-induced increases in copper resistance or rotor eddy currents due to stator current-induced fluctuation in magnetic field, we include a constant k_{loss} which we assume is uniform across motors of a given topology:

$$P_{loss} = k_{loss} \left(\frac{\tau_{motor}}{k_m} \right)^2. \tag{15}$$

The motor constant k_m can be expressed as in [28]:

$$k_m = \frac{k_{tq}}{\sqrt{R_\phi}} = \sqrt{\frac{3}{2}} \frac{k_{t\phi}}{\sqrt{R_\phi}}, \tag{16}$$

where k_{tq} is the motor torque constant in the quadrature axis, $k_{t\phi}$ is the torque constant per phase, and R_ϕ is the line-to-neutral resistance of one phase.

We approximate the phase torque constant $k_{t\phi} = f(R_o, k_d, B_g, N_p)$ and phase resistance $R_\phi = f(R_o, k_d, B_g, N_p, k_p)$ using design equations 6.64 and 6.72, respectively, from [26].

3) Maximum motor torque: The maximum torque that a BLDC motor can produce is generally limited by thermal losses in the stator. Wearable robots often have target trajectories with high peak torques and low duty ratios, so we set a limit on the maximum instantaneous torque produced by the motor, rather than steady-state or RMS torque. In this transient case, we assume that heat in the stator coils is generated much faster than it can be dissipated, and therefore treat the stator as an insulated thermal mass. This produces a simple relationship between the loss power generated by the stator P_{loss} (equation 15) and the rate of temperature increase of the stator copper:

$$P_{loss} = m_{cu} c_{cu} \dot{T}, \tag{17}$$

where c_{cu} is the specific heat capacity of copper and m_{cu} is the mass of copper in the stator. m_{cu} can be approximated by combining equations (1) - (3), yielding:

$$m_{cu} = k_p t_s (a_{slot} + a_{end}) \rho_{cu}. \tag{18}$$

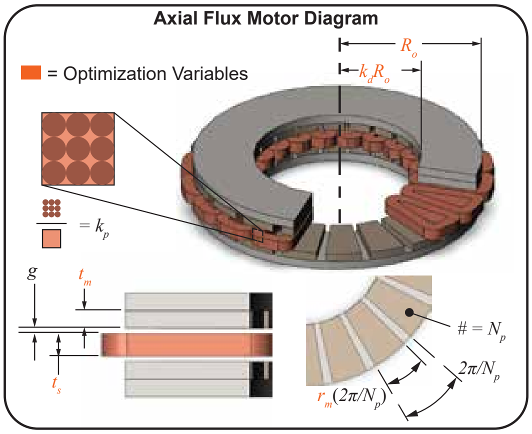

Fig. 2. Diagram of dual-rotor axial flux motor showing motor geometry. Optimization variables are denoted in red. N_p is a function of gear ratio G_r and maximum motor angular velocity $\max(\omega_{act})$ (equation 5).

Combining equations (15) and (17) yields an expression for maximum instantaneous motor torque τ_{max}:

$$\tau_{max} = k_m \sqrt{\frac{m_{cu} c_{cu} \dot{T}_{max}}{k_{loss}}}, \tag{19}$$

where $\dot{T}_{max}$ is the maximum allowable rate of temperature rise in the stator. We assume that this is a constant dictated by the insulation material surrounding the copper.

III. MODEL VALIDATION & EXPERIMENTAL CHARACTERIZATION

In this section, we validate our models for m_{motor}, τ_{max}, and P_{batt} using a mixture of datasheet inspection and experimental methods. For ease of measurement, P_{batt} is used as a proxy for m_{batt} (see equations 6 - 9). We first estimate the values of manufacturing-specific constants necessary to calculate m_{motor}, τ_{max}, and P_{batt}. We then test the accuracy of m_{motor} and τ_{max} against datasheet-predicted values. To validate P_{batt}, we first experimentally measure gear efficiency for three different gear ratios and fit the data to equation 13 to estimate η_0. Then, we measure the accuracy of our model prediction of electrical power draw in both steady-state and dynamic actuation profiles.

A. Estimation of Constants and Validation of Motor Mass

Our model depends on four constants that must be adjusted to a specific motor manufacturing process: maximum back iron flux density B_{bi} , conductor packing factor k_p, loss factor k_{loss}, and maximum rate of temperature rise $\dot{T}_{max}$. We can infer the value of these constants by comparing certain 'reference parameters' that are reported by both our model and by manufacturer datasheets.

For each constant, the best-fit value between the model and 22 datasheets was calculated using the Levenberg-Marquardt algorithm. Datasheets were supplied by a PCB motor manufacturer (ECM PCB Stator, MA, USA) and were chosen to cover a wide range of rated speeds, output powers, and efficiencies.

B_{bi} was fit using the reported value for back-iron thickness t_{bi} as the reference parameter (equation 4). k_p was fit using the

This article has been accepted for publication in IEEE/ASME Transactions on Mechatronics. This is the author's version which has not been fully edited and content may change prior to final publication. Citation information: DOI 10.1109/TMECH.2026.3662305

reported value for motor constant k_m as the reference parameter (equation 16). k_{loss} was fit using the reported value for loss power $(P_{elec} - P_{mech})$ as the reference parameter (equation 15). $\dot{T}_{max}$ was fit using reported values for maximum torque τ_{max} as the reference parameter (equation 19).

We then calculated the predicted motor mass using the best-fit values for B_{bi} and k_p for all 22 motor datasheets and compared the motor mass prediction to the datasheet value.

B. Gear Efficiency & Battery Power Validation

In this section, we describe the experimental prototypes and test apparatus, then use them to measure gear efficiency η and electrical power drawn from the battery P_{batt}.

1) Prototype Fabrication: The test motor was fabricated by ECM PCB Stator (MA, USA) using a 15-slot, 20-pole arrangement, N42 grade magnets, and the following geometric parameters: $R_0 = 42.5$ mm, $k_d = 0.61$, $r_m = 0.75$, $t_m = 1.50$ mm, and $t_s = 1.28$ mm. The coil winding pattern was proprietary and unknown to the authors, so only winding-independent metrics can be modeled for this prototype. The frame of the cycloid gear (housing and outer ring) was machined from 6061-T6 aluminum. The meshing components of the cycloid gear (eccentric shaft, cycloid disk, and cycloid ring insert) were cut by wire EDM out of 7075-T6 aluminum (selected for its high strength to weight ratio) to a tolerance of ±0.013 mm and a surface finish of 0.8 µm Ra. The profile of the cycloid was generated with the roller pitch radius reduced by 0.05 mm to establish nominal clearance between the disk and the outside rollers, as per [16]. The outside roller pitch diameter was 70 mm and the thickness of all meshing components was 4 mm. The gear was coated with a molybdenum grease (XHP 222 Special, Exxon Mobil, USA). Three sets of meshing components were made with gear ratios of 20:1, 28:1, and 35:1 in order to develop a relationship between gear ratio and efficiency.

2) Custom Benchtop Dynamometer: To characterize the device, we used a custom benchtop dynamometer that includes two torque sensors and an absorber motor (Fig. 3). The dynamometer is composed of several modules: the PCB motor under test, a rotary torque sensor (TRS300, Futek, USA), a cycloid gear module, a full actuator module (PCB motor and cycloid gear), and an absorber motor module. The absorber module includes a BLDC motor (AK10-9 V2.0, Cubemars, China) which is mounted to the frame of the dynamometer through a reaction torque sensor (TFF350, Futek, USA), allowing for torque and position measurements of the output shaft. Different configurations of this dynamometer allow for multiple tests to be performed, detailed below.

3) Data Collection & Processing: All data collected on the custom dynamometer were recorded on a Real-time Target Machine (Baseline real-time target machine, Speedgoat, Switzerland) at 1000 Hz. Electrical power was calculated as the product of DC bus voltage and current as reported by the motor driver (ODrive Pro, ODrive Robotics, USA) over a Controller Area Network (CAN) connection to the Real-time Target Machine. All mechanical power data were calculated as the product of torque and angular velocity. Torque data was collected from each load cell as an analog voltage signal through an amplifier (CSG110, Futek, USA). Velocity data was collected from the commutation encoders on each motor and reported by each motor's respective driver over CAN. All data were digitally filtered post-collection with an 8th-order zero-phase Butterworth filter with a half-power frequency of 15 Hz to remove noise.

Three types of tests were performed on the dynamometer: steady-state ($\alpha = 0$), dynamic ($\alpha \neq 0$), and open-loop frequency response. For the steady-state tests, the rotary torque sensor was connected between the test motor and the cycloid gear, and the absorber module was connected to the output ring of the cycloid gear (Fig. 3 A). Steady-state tests were repeated for each gear ratio. For the dynamic tests, the actuator module was used instead of the test motor module, and the cycloid gear module was removed. This change ensured that inertial torques due to accelerations were accurately represented and measured for the dynamic tests. (Fig. 3 B). For the open-loop frequency response tests, the actuator module was connected directly to the torque sensor of the output module, which was mechanically grounded to the frame, preventing rotation of the outer ring of the gear (Fig. 3 C).

For both static and dynamic tests, velocity was commanded by the test motor while a constant torque was commanded by the absorber motor. for the static tests, constant velocities were commanded, while for the dynamic tests, velocity commands were sent as a sine wave with 30 rad/s frequency with a commanded peak velocity.

For the steady-state tests, the absorber was controlled to torques of -20, -12, -4, 4, 12, & 20 N·m and the test motor was controlled to 50, 100, and 150 rad/s, creating a grid of 18 conditions per gear (note that data loss occurred for four conditions with the $28:1$ gear ratio actuator at 150 rad/s). The input and output mechanical powers were averaged over the last five seconds of each condition. For the dynamic tests, the absorber was controlled to torques of -12, -4, 0, 4, & 12 N·m (the ±20 N·m conditions were removed due to the capacity of the rotary torque sensor, and a 0 N·m condition was added to isolate inertial loads) and the test motor was controlled to 50, 100, and 150 rad/s, creating a grid of 15 conditions. the last five seconds of each condition were recorded and the maximum, RMS, and mean values of power were calculated. For the frequency response tests, the test motor was commanded to apply sinusoidal quadrature current with an amplitude of ±20 A. Fifty frequencies were swept between 1 and 100 Hz, and bode plots were generated for the transfer from quadrature current to output torque. Tests were repeated three times per gear ratio and averaged in Fig.3 C.

C. Results

1) Motor Model Validation with Datasheets: After fitting, the model constants and 95% Confidence Intervals (CI95) were $B_{bi} = 1.43$ T (CI95: 1.40-1.46), $k_p = 0.46$ (CI95: 0.42-0.50), $k_{loss} = 1.44$ (CI95:1.37-1.51), $\dot{T}_{max} = 31.91$ °C/s (CI95: 23.71-40.10). Using these best-fit parameters, the values for m_{motor}, k_m, J, and τ_{max} were modeled and compared against the datasheets. J was inferred from the datasheet as $J = t_c k_m^2$

This article has been accepted for publication in IEEE/ASME Transactions on Mechatronics. This is the author's version which has not been fully edited and content may change prior to final publication. Citation information: DOI 10.1109/TMECH.2026.3662305

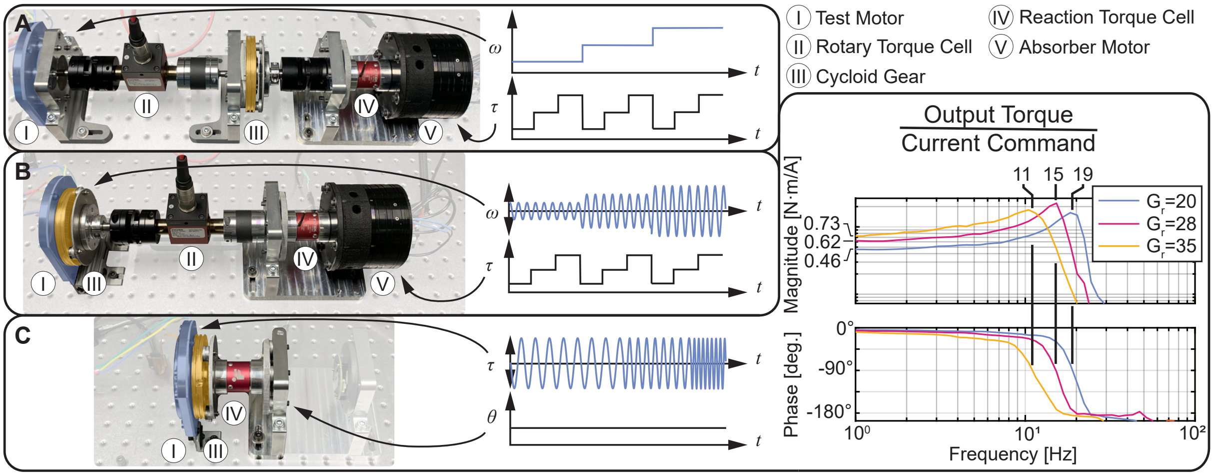

Fig. 3. A) Custom dynamometer arrangement used for steady-state ($\alpha = 0$) actuator testing (top). The test motor is driven to a series of constant speeds while the absorber iterates through constant resistive torques (bottom). B) The same dynamometer with the rotary torque sensor removed to enable dynamic ($\alpha \neq 0$) testing. The absorber motor iterates through the same constant torques while the test motor iterates through a series of sine wave magnitudes ($f = 30$rad/s). (C) Open-loop frequency response of the actuator with 20:1, 28:1, and 35:1 gear ratio transmissions for frequency range 1 Hz to 100 Hz.

where t_c is the time constant of the motor. The accuracy of J was analyzed instead of t_{bi} because of its relevance in calculating motor performance (equation 12). The accuracy of the models for these parameters is summarized in Table I.

2) Experimental Results: For each gear ratio, the measured gear efficiencies η of the steady-state test conditions were used to calculate a best-fit bearing efficiency η_0 using equation (13) and the following model given mechanical power at the gear output P_{out} and mechanical power at the gear input P_{in}:

$$P_{out} = P_{in}\eta^{\mathrm{sgn}(P_{in})}.$$

The resulting best-fit value for bearing efficiency was $\eta_0 = 0.9937$ (95% CI: $0.9925 - 0.9949$), corresponding to predicted [actual] gear efficiencies of 0.88 [0.87], 0.84 [0.85], and 0.81 [0.82] for the $20:1$, $28:1$, and $35:1$ gear ratios, respectively. Gear mass was also found to be approximately constant, with respective masses of 207 g, 211 g, and 214 g for the three tested gear ratios.

The accuracy of predicted power draw can be captured through four models. The accuracy of P_{loss} in the absence of accelerations is given by the steady-state tests and is denoted P_{SS} in Table I. The accuracy of P_{batt} during dynamic movement can be measured with the scalar metrics of $\max(P_{batt})$, $\mathrm{RMS}(P_{batt})$, and $\mathrm{mean}(P_{batt})$ to reflect their use in approximating m_{batt} (equations 6 - 9). Model root-mean-squared error (RMSE), R^2, and mean absolute percent accuracy (with 95% Confidence Interval) across dynamic conditions are summarized in Table I.

Open-loop frequency response results shown in Fig. 3 C show approximate actuator torque constants (1 Hz transfer amplitude) of 0.46, 0.62, and 0.73 N·m/A, with resonant peaks at 19, 15, and 11 Hz for the $20:1$, $28:1$, and $35:1$ gear ratios, respectively. These are safely above the approximately 3.5 Hz bandwidth of human ankle torque during walking [29].

TABLE I
SUMMARY OF MODELING VALIDATION RESULTS FOR 22 MOTOR DATASHEETS (TOP) AND THREE GEAR RATIOS (BOTTOM)

Variable	RMSE	R^2	% Accuracy (CI95)
m_{motor}	43.2 g	0.997	95.9 (95.0 - 96.8)
k_m	.019 N·m / $\sqrt{\mathrm{W}}$	0.976	91.5 (89.7 - 93.3)
J	1274.1 g·cm^2	0.999	96.4 (95.4 - 97.4)
τ_{max}	1.89 N·m	0.846	73.6 (67.7 - 79.4)
η	0.010	0.853	82.2 (77.9 - 86.6)
P_{SS}	31.75 W	0.858	75.9 (69.9 - 81.9)
$\max(P_{batt})$	19.75 W	0.931	86.3 (80.4 - 92.2)
$\mathrm{RMS}(P_{batt})$	7.41 W	0.958	87.9 (83.0 - 92.7)
$\mathrm{mean}(P_{batt})$	6.04 W	0.941	83.0 (78.0 - 88.1)

IV. APPLICATION CASE STUDY: ANKLE EXOSKELETON FOR POST-STROKE WALKING

In this section, we show an example of how the proposed design framework can be used to optimize 'sized' actuators for a wearable ankle exoskeleton for post-stroke walking assistance. Choosing a number of actuator sizes presents a tradeoff: Having fewer sizes results in higher average mass borne by the user, while having more sizes increases the costs and logistical difficulty of manufacturing the device. First, we describe how the target performance trajectories were generated for each individual. Then, we formulate the optimization problem that takes the performance trajectories as inputs and outputs motor geometry and gear ratio. We then group the performance requirements to create actuator sizes to explore the effect of sized actuators on average system mass.

A. Performance Trajectory Generation

1) Data Collection and Torque Requirement Identification: To identify the required torques, speeds, and accelerations for each subject, we first captured walking data of 12 unimpaired adults walking at controlled walking speeds of 0.5, 0.75, 1.0, 1.25, 1.5, and 1.75 m/s on an instrumented treadmill (data from [30]) as well as 19 stroke survivors (14 from [31] plus 5 additional participants) walking overground on an instrumented indoor track at comfortable walking speeds. Informed consent was obtained from all participants.

The motion of markers was captured using Qualisys, and kinematics and kinetics were computed using Visual 3D (C-Motion Inc., Canada). To establish a healthy reference gait, we

This article has been accepted for publication in IEEE/ASME Transactions on Mechatronics. This is the author's version which has not been fully edited and content may change prior to final publication. Citation information: DOI 10.1109/TMECH.2026.3662305

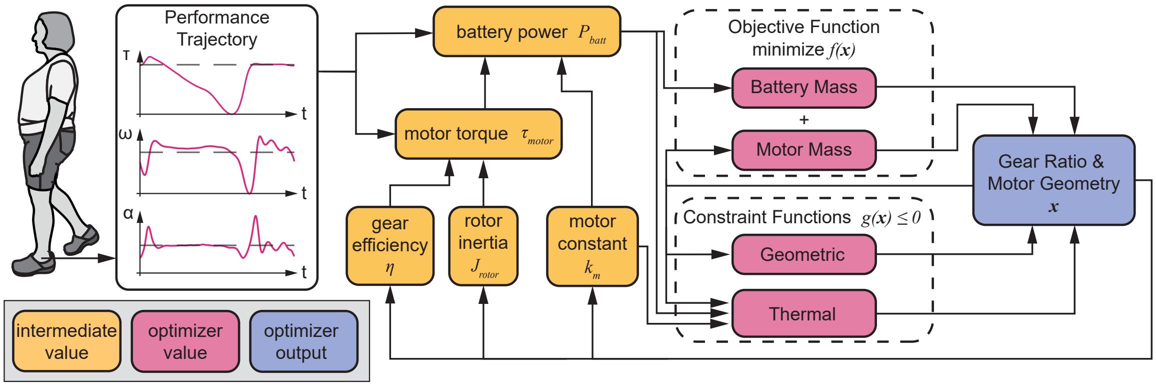

Fig. 4. Diagram of actuator optimization process. Gear ratio and motor geometry are optimized for a given performance trajectory dictated by measured biomechanics. Higher performance requirements increase motor torque and power, which in turn determine the battery mass and thermal condition of the motor. Motor geometry determines the motor mass as well as determining intermediate values η, J_{rotor}, and k_m, which int turn influence τ_{motor} and P_{batt}.

first nondimensionalized the ankle torque, ankle angular velocity, and ankle angular accelerations of each unimpaired subject walking at controlled speeds according to [32]. We then averaged the waveforms for each subject and subsequently took the average across subjects at each speed to establish six normalized sets of torques, speeds, and accelerations at different walking speeds. Walking speed was then normalized to the Froude number for each of these mean walking speeds.

2) Assistance Profile Generation: For each stroke survivor, their comfortable walking speed Froude number was calculated, and the reference nondimensional waveforms for ankle torque, speed, and acceleration were linearly interpolated to arrive at the subject-specific nondimensional waveforms. These waveforms were then converted back into torque, velocity, and acceleration units using each participant's mass and leg length.

The target actuator velocity and acceleration were set equal to the unimpaired reference ankle velocity and acceleration, respectively. To set actuator torque requirement, we scaled the unimpaired reference torque such that the peak torque was equal to half the difference between the average peak paretic torque over five strides and the peak healthy reference torque:

$$\tau_{actuator} = 0.5\tau_{unimpaired}\left(1 - \frac{\text{mean}(\max(\tau_{paretic}))}{\max(\tau_{unimpaired})}\right) \tag{20}$$

This scaling represents a rough approximation for half the torque 'deficiency' in the paretic leg that the actuator would compensate for. The optimizer was run for each participant, and optimized gear ratio, motor geometry, motor mass, battery mass, and motor performance metrics were recorded.

B. Optimizer Formulation

The minimization of the actuator and battery mass was formulated as a constrained optimization problem:

$$\begin{aligned} \min_{\mathbf{x}} \quad & f(\mathbf{x}) \\ \text{subject to} \quad & g(\mathbf{x}) \leq 0 \\ & h(\mathbf{x}) = 0 \\ & \mathbf{x} \in \Re^6, \end{aligned}$$

with objective function $f(\mathbf{x})$:

$$\begin{aligned} f(\mathbf{x}) &= m_{motor}(\mathbf{x}, \omega_{act}(t)) \\ &\quad + m_{batt}(\mathbf{x}, \tau_{act}(t), \omega_{act}(t), \alpha_{act}(t)) \\ \text{for} \quad & t = 0, \ldots, t_{end}, \end{aligned}$$

where $\tau_{act}(t)$, $\omega_{act}(t)$, and $\alpha_{act}(t)$ are the set of desired actuator torques, velocities, and accelerations across time $t = 0, \ldots, t_{end}$. The design variables $\mathbf{x}$ were defined as:

$$\mathbf{x} = \left[G_r, R_o, k_d, r_m, t_m, t_s\right]^T, \tag{21}$$

where G_r is the cycloid gear ratio, R_o is the motor outer radius, k_d is the ratio of the motor inner diameter to the outer diameter, r_m is the fraction of the magnet pitch angle taken up by the magnet (magnet fraction), t_m is the magnet thickness, and t_s is the stator thickness. Note that gear mass was assumed to be constant at 210 g. A visualization of the optimization process is shown in Fig. 4. To meet actuator manufacturing limits, the design variable space $\mathbf{x} \in \mathcal{X}$ was bounded by a series of design constraints (see Table II).

TABLE II
OPTIMIZER DESIGN VARIABLE LIMITS

Variable	Min. Value	Initial Value	Max. Value	Units
G_r	10	30	100	-
R_o	10	40	75	mm
k_d	0	0.7	1	-
r_m	0.7	0.8	1	-
t_m	1	2	5	mm
t_s	0	1	2.4	mm

In order to prevent the actuator from reaching its thermal limit, a functional constraint was imposed to limit motor torque $\tau_{motor}(\mathbf{x}, \tau_{act}, \omega_{act}, \alpha_{act})$ for a given torque, speed, and acceleration trajectory:

$$\begin{aligned} g_t(\mathbf{x}) &= \tau_{motor}(\mathbf{x}, \tau_{act}(t), \omega_{act}(t), \alpha_{act}(t)) - \tau_{max} \\ \text{for} \quad & t = 0, \ldots, t_{end}, \end{aligned}$$

where τ_{max} is calculated as in equation 19.

The optimization problem was solved using the MATLAB (MathWorks, USA) Optimization Toolbox `fmincon` function with an interior-point algorithm, using a maximum of 2000 iterations. Table III lists the constants used for optimization.

This article has been accepted for publication in IEEE/ASME Transactions on Mechatronics. This is the author's version which has not been fully edited and content may change prior to final publication. Citation information: DOI 10.1109/TMECH.2026.3662305

TABLE III
VALUES OF CONSTANTS USED IN ACTUATOR MASS OPTIMIZATION.

Variable	Description	Value	Units
t_{charge}	Desired run time of actuator	2.0	hr
C_{max}	Max. discharge rate of Li-ion battery	5.0	hr^{-1}
C_{cont}	Rated discharge rate of Li-ion battery	1.0	hr^{-1}
ρ_{batt}	Energy density of Li-ion battery	0.3	W·h/g
B_{bi}	Maximum back-iron flux density	1.43	T
k_p	Conductor packing factor	0.46	-
k_{loss}	Electrical power loss factor	1.44	-
$\dot{T}_{max}$	Maximum temperature rise rate	31.91	°C/s.
η_0	Cycloid bearing efficiency	0.9937	-
k_w	Winding factor	0.866	-
g	Air gap distance	0.6	mm

C. Actuator Sizing

Ideally, optimal actuator geometry and mass would be computed for each participant's performance requirements. In practice, it may not be feasible to fabricate individually-sized actuators and batteries. Therefore, we have investigated designing sized components that are optimized for subgroups of participants. Three scenarios were tested: a one-size-fits-all actuator and group-sized batteries; group-sized actuators and a one-size-fits-all battery; and group-sized actuators and group-sized batteries. Participants were divided into even quantile subgroups according to individually optimized system mass.

At each optimization iteration, motor and battery mass were computed using the combined performance trajectory for all participants within that group. For the sized-battery, single-actuator scenario, at each iteration, the optimizer calculated a single actuator that would satisfy the performance requirements across all groups, then calculated the battery size for each group based on that single actuator. For the sized-actuator, single-battery scenario, the actuator and battery mass were calculated for each group, then the largest battery mass was used for all groups for each iteration. For the sized-actuator, sized-battery scenario, the actuator and battery mass were individually calculated for each group at each iteration. For all scenarios, the optimizer cost function was the average of the combined motor and battery mass across groups.

D. Optimization Results

1) Individual Optimization Results: Optimal actuator geometry varied considerably across individual participants for most design variables. The most consistent variables were k_d, which varied from 0.537 to 0.612, r_m, which consistently converged on the lower limit of 0.7, and t_s, which ranged from 1.61 mm to 2.40 mm, but with a mean value close to its upper limit of 2.36 mm. Other variables varied much more, with R_0 ranging from 13.7 mm to 39.4 mm, and t_m from 1.36 mm to 2.52 mm. The individually-optimized combined motor and battery mass ranged from 26 g to 440 g with a mean of 194 g, demonstrating the necessity of sized actuators.

Analysis of optimizer results using Pearson Correlation Coefficient (PCC) revealed strong relationships between performance requirements and optimized actuator parameters (Fig. 5A). Most notably, maximum demanded acceleration was negatively correlated with optimal gear ratio G_r (PCC = -0.8454), and maximum demanded torque was positively correlated with optimal motor constant k_m (PCC = 0.8993).

To validate the robustness of the optimizer, it was tested for its sensitivity to variations in fit constants (B_{bi}, k_p, k_{loss}, $\dot{T}_{max}$, η_0, g) and starting parameters within the feasible range. Fit constants were varied by $\pm 20\%$ using Latin Hypercube Sampling (LHS) (N=100), and Standardized Regression Coefficients (SRC) were calculated, revealing moderate sensitivity to k_p (SRC = -0.76) and B_{bi} (SRC = -0.46), and low sensitivity ($|\mathrm{SRC}| < 0.25$) to all other constants. Starting parameters were varied within their feasible range using LHS (N=1000) to identify local minima or convergence issues. Three runs failed to converge, 969 runs converged within 1% of the lowest total mass value, and the worst feasible run converged to 12.9% higher mass than the lowest run, showing overall high stability for the optimizer.

2) Sizing Results: All three methods of sizing (sizing the battery, sizing the motor, and sizing both) resulted in lower overall system masses than the optimized 672 g one-size-fits-all actuator, with an apparent diminishing returns effect as the number of sizes increased (Fig. 5 B). When both the actuator and battery were sized, the average motor and battery mass decreased by 306 g when three sizes were used instead of one size, 78 g when five sizes were used instead of three, 19 g when seven sizes were used instead of five, and 32 g when nine sizes were used instead of seven.

V. DISCUSSION

In this work, we present the design and modeling of a thin, lightweight robot actuator and propose an optimization-based design framework for tailoring the actuator to specific performance requirements. The actuator architecture, based on a PCB motor and cycloid gear, allows for a wide range of motor sizes and gear ratios to be implemented with minimal change to actuator thickness. We optimize gear ratio and motor geometry to minimize the combined weight of the motor and battery based on target performance requirements along with manufacturing and thermal constraints. Finally, we show how this design framework can be used to create multiple sizes of actuators for segments of a target population to further reduce the weight of the device depending on individual requirements.

A. Actuator Design

The actuator design proposed in this paper achieves high torque density in a slim, lightweight package. As a high-level comparison to other actuator topologies, we use the single-size actuator from this study, which has optimal design variables of [26, 45.8 mm, 0.62, 0.70, 2.7 mm, 2.4 mm], and compare it against other wearable actuators developed for ankle assistance in Table IV.

This comparison demonstrates the difficulty of balancing torque capacity, weight, and thickness for wearable actuators.

This article has been accepted for publication in IEEE/ASME Transactions on Mechatronics. This is the author's version which has not been fully edited and content may change prior to final publication. Citation information: DOI 10.1109/TMECH.2026.3662305

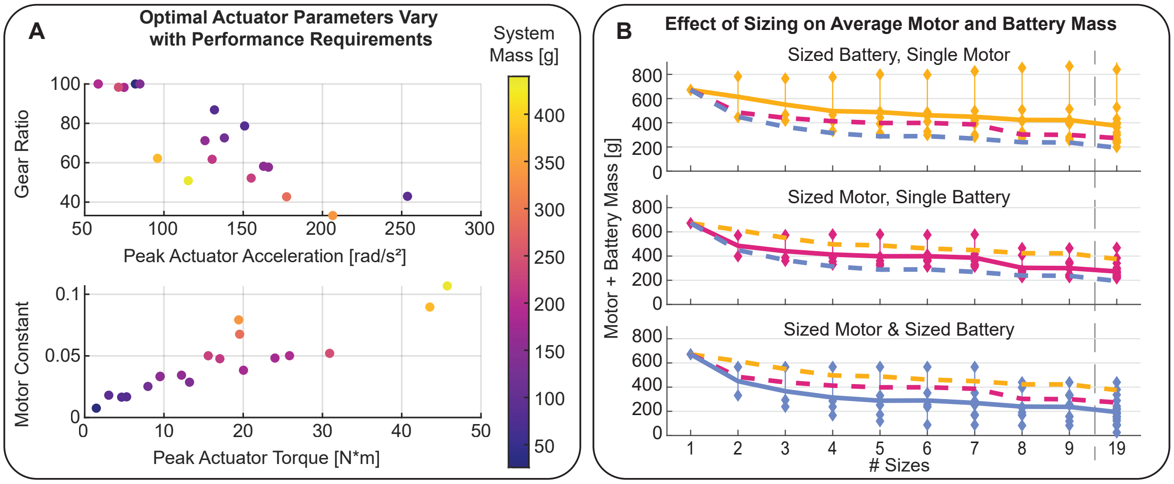

Fig. 5. A) Individually-optimized actuator gear ratio and motor constant correlated with peak demanded actuator acceleration and torque, respectively. Each dot represents an individual's optimized result, while the color of the dot denotes the resulting optimized combined motor and battery mass. B) Combined motor and battery masses across participants (n=19) as a function of number of sizes. Three conditions were compared: sizing only the battery (orange, top), sizing only the actuator (pink, middle), and sizing both together (blue, bottom). The mass of each size is denoted by a diamond, and the average across groups is marked with a solid or dashed line. The average lines for each sizing scenario are repeated across subplots for comparison. Sizing both the actuator and battery resulted in the greatest weight savings, and all conditions result in diminishing weight savings with increased number of sizes.

TABLE IV
COMPARISON OF ANKLE EXOSKELETON ACTUATORS

Actuator Name	Motor Topology	Gear Type	Gear Ratio	Actuator Mass [g]	Peak Torque [N·m]	Peak Torque Density [N·m/kg]	Thickness [mm]
PCB + Cycloid (This study)	Dual Rotor Axial Flux	Cycloid	26	~600	45	75	33
Mooney et al. 2014 [5]	Inrunner Radial Flux	Multiple	120	~1000	120	120	<300*
Slade et al. 2022 [7]	Outrunner Radial Flux	Multiple	45	~600	54	~90	~75
Bae et al. 2018 [6]	Inrunner Radial Flux	Multiple	371**	~750	24**	~32	63
Sarkisian et al. 2025 [33]	Inrunner Radial Flux	Multiple	200-425	708	46	65	24
Zhao et al. 2024 [23]	Outrunner Radial Flux	Planetary	9	584	30	51	>40

*Unreported, varies with ankle angle. **Assumed lever arm about the ankle joint of 80 mm.

The actuators used by Mooney et al. [5] and Slade et al. [7] attain higher peak torque density than the actuator proposed in this work by extending the lever arm about the ankle joint, dramatically increasing the protrusion of the device away from the body. The soft exosuit developed by Bae et al. [6] mounts the actuator on the lower back to minimize thickness near the ankle, but its high gear reduction and low efficiency ultimately result in low torque density and a somewhat thick proximal actuator. Sarkisian et al. [33] developed a tightly integrated high-gear-ratio drivetrain that achieves high torque density in a very thin package, and uses active torque compensation and an in-line spring to add some backdrivability at the expense of some control bandwidth. Zhao et al. [23] opted for a low-gear-ratio design to target passive backdrivability and high control bandwidth, at the expense of lower torque density and higher thickness.

B. Modeling

The models for m_{motor} and P_{batt} had relatively high R^2 values, showing that the proposed model could reliably approximate the motor mass and power draw of a cycloid gear and PCB motor actuator given the motor geometry and performance requirements. In modeling power draw, it should be noted that power draw was reported directly from the motor driver with unknown accuracy, and the introduction of k_{loss}, while consistent across the tested actuators, may not be a valid approximation for other motor and gear configurations. Further validation of power draw estimation may be needed for future research. The lowest R^2 values were associated with the model for gear efficiency η and peak motor torque τ_{max}. The low R^2 value associated with η is likely due to manufacturing inconsistencies in the cycloid gear prototypes fabricated for this study. The low R^2 value for τ_{max} is likely due to the highly simplified thermal model used in this paper.

It should be noted that motor mass, motor constant, rotor inertia, and gear efficiency are all values often reported on component datasheets. The model presented in this work was designed to be used to design custom motors, similar equations can be used to compare actuators using off-the-shelf components [18], [19], [27], [34], allowing comparison across motor and gear topologies.

C. Optimization & Sizing

The proposed optimizer formulation provides a general, deterministic design framework for minimizing weight given an application's performance requirements. It should be noted that the optimal performance trajectory for achieving a desired biomechanical outcome may differ from the trajectories proposed here and will depend on an eventual use case, operating environment, and population.

The case study in this paper revealed the potential benefits of creating 'sized' actuators for exoskeletons, rather than

This article has been accepted for publication in IEEE/ASME Transactions on Mechatronics. This is the author's version which has not been fully edited and content may change prior to final publication. Citation information: DOI 10.1109/TMECH.2026.3662305

pursuing a one-size-fits-all approach. When the actuator and battery were sized together, the optimizer showed an average weight savings of 384 g by using five sizes of actuator and battery, which is over half of the predicted mass of 672 g of a ‘one-size-fits-all’ motor and battery.

Sizing either the actuator or the battery also yields weight savings to a lesser extent. With multiple actuator sizes, each motor is smaller and requires less power than if a single actuator were used, thus requiring a smaller battery for each. When the battery is sized, the optimal single actuator size is smaller, and the optimal battery size becomes larger for some of the population while it becomes substantially lower for other segments of the population, thereby reducing average combined mass. In our case study, sizing only the actuator saved more mass than sizing only the battery.

While creating individualized sizes of motor and battery leads to optimal weight savings, this must be balanced with the economics of manufacturing those sizes. Although this actuator topology is particularly suitable for sizing and low-volume manufacturing, individualized data collection may be impractical. Our case study results indicate that a lower number of sized actuators can capture the majority of the weight saving benefits of individually-sized actuators while reducing the burden of collecting data and manufacturing customized actuators for every user. With only five sizes of actuator, the average mass saving was 80% of the individually-optimized weight savings, and with eight sizes the average mass saving was 91% of the individualized optimum.

The main limitations of this study are the limited number of stroke survivors ($N = 19$) and the lack of consideration for how the actuator mass may affect the required performance trajectory for an individual. Using data from more individuals would allow us to capture more of the heterogeneity present in stroke survivors when computing subgroups for generating sized actuators. Furthermore, a better understanding is needed of how the added mass of an exoskeleton may change an individual’s gait, and therefore change the required performance trajectory for the actuator. In the future, a model of this could be integrated into the design framework. Another consideration for expansions of this model could be inclusion of manufacturing tolerances or sensitivity analysis, particularly for parameters like air gap distance which are very small (< 1 mm) and difficult to control precisely.

Other studies have proposed control strategies for an exoskeleton actuator such as energy-shaping controllers [23], torque/admittance controllers [33], position/admittance controllers [35], etc. The eventual controller selection will also impact actuator requirements. However, the design framework presented in this study is controller agnostic, as it only requires a performance trajectory when optimizing actuator mass. Furthermore, the required performance trajectories tested in this work cover a range of torques, accelerations, and velocities; a promising indicator that the design framework is suitable for a variety of control strategies.

VI. CONCLUSION

In this paper, we proposed the design, modeling, and optimization of axial flux PCB motor and cycloid gear actuators for wearable robots. The proposed design architecture is able to accommodate a wide range of gear ratios and PCB motor geometries while maintaining a thickness of only ∼33 mm. This approach is easily transferable to other joints or other robotic applications like mobile robotics where it is critical to minimize size and weight.

We then proposed models for motor mass, battery mass, and maximum torque, which were used in the formulation of an optimization problem that uses performance requirements as model inputs, then optimizes actuator geometry to minimize the combined weight of the motor and battery. This optimizer could also be adapted to design optimal actuators for other use cases simply by modifying the cost function, making it potentially useful for any application with known transient performance trajectories.

Finally, a case study of an ankle exoskeleton for post-stroke walking assistance revealed the mass-saving potential of using sized wearable actuators. We optimized motor geometry and gear ratio for 19 individuals post-stroke. The one-size-fits-all optimal gear ratio was 26, and optimal combined motor and battery mass was 672 g. When instead five sizes were used, the optimal gear ratios ranged from ∼33 to ∼62, with motor and battery masses between ∼119 g to ∼567 g.

Future work will integrate the optimized actuator geometry into assistive wearable robots. We will also continue to refine the design of the actuator to reduce mass and thickness. The model presented in this work could also be expanded to compare different optimized motor and gear topologies to explore other actuator topologies for other robotic applications.

REFERENCES

[1] I. Safaz, F. Tok, I. Tugcu, H. Turk, E. Yasar, and R. Alaca, “Use and Abandonment Rates of Assistive Devices/Orthoses in Patients with Stroke,” *Gulhane Medical Journal*, vol. 57, no. 2, p. 142, 2015.

[2] C. Duclos, S. Nadeau, N. Bourgeois, L. Bouyer, and C. L. Richards, “Effects of walking with loads above the ankle on gait parameters of persons with hemiparesis after stroke,” *Clinical Biomechanics*, vol. 29, no. 3, pp. 265–271, 2014.

[3] F. Gemperle, C. Kasabach, J. Stivoric, M. Bauer, and R. Martin, “Design for wearability,” *Digest of Papers. Second International Symposium on Wearable Computers (Cat. No.98EX215)*, pp. 116–122, 1998.

[4] A. J. Veale and S. Q. Xie, “Towards compliant and wearable robotic orthoses: A review of current and emerging actuator technologies,” *Medical Engineering & Physics*, vol. 38, no. 4, pp. 317–325, 2016.

[5] L. M. Mooney, E. J. Rouse, and H. M. Herr, “Autonomous exoskeleton reduces metabolic cost of human walking during load carriage,” *Journal of NeuroEngineering and Rehabilitation*, vol. 11, no. 1, p. 80, 2014.

[6] J. Bae, C. Siviy, M. Rouleau, N. Menard, K. O’Donnell, I. Geliana, M. Athanassiu, D. Ryan, C. Bibeau, L. Sloot, P. Kudzia, T. Ellis, L. Awad, and C. J. Walsh, “A Lightweight and Efficient Portable Soft Exosuit for Paretic Ankle Assistance in Walking After Stroke,” *2018 IEEE International Conference on Robotics and Automation (ICRA)*, vol. 00, pp. 2820–2827, 2018.

[7] P. Slade, M. J. Kochenderfer, S. L. Delp, and S. H. Collins, “Personalizing exoskeleton assistance while walking in the real world,” *Nature*, vol. 610, no. 7931, pp. 277–282, 2022.

[8] D. D. Molinaro, K. L. Scherpereel, E. B. Schonhaut, G. Evangelopoulos, M. K. Shepherd, and A. J. Young, “Task-agnostic exoskeleton control via biological joint moment estimation,” *Nature*, vol. 635, no. 8038, pp. 337–344, 2024.

[9] H. Zhu, C. Nesler, N. Divekar, V. Peddinti, and R. D. Gregg, “Design Principles for Compact, Backdrivable Actuation in Partial-Assist Powered Knee Orthoses,” *IEEE/ASME Transactions on Mechatronics*, vol. 26, no. 6, pp. 3104–3115, 2020.

This article has been accepted for publication in IEEE/ASME Transactions on Mechatronics. This is the author's version which has not been fully edited and content may change prior to final publication. Citation information: DOI 10.1109/TMECH.2026.3662305

[10] A. Cavagnino, M. Lazzari, F. Profumo, and A. Tenconi, "A Comparison Between the Axial Flux and the Radial Flux Structures for PM Synchronous Motors," *IEEE Transactions on Industry Applications*, vol. 38, no. 6, p. 1517, 2002.

[11] J. F. Gieras, R.-J. Wang, and M. J. Kamper, *Axial Flux Permanent Magnet Brushless Machines*, 2nd ed. Springer Science & Business Media, 2008.

[12] M. Waldhof, A. Echle, and N. Parspour, "A Novel Drive Train Concept for Personalized Upper Body Exoskeletons with a Multiphase Axial Flux Machine," *2019 IEEE International Electric Machines & Drives Conference (IEMDC)*, vol. 00, pp. 2160–2166, 2019.

[13] M. Waldhof, I. Wochner, K. Stollenmaier, N. Parspour, and S. Schmitt, "Design and Scaling of Exoskeleton Power Units Considering Load Cycles of Humans," *Robotics*, vol. 11, no. 5, p. 107, 2022.

[14] F. Yi, C. Zhang, S. Chen, S. Qiu, H. Zhang, Q. Du, W. Wang, and G. Yang, "A compact actuator for lower-limb exoskeletons with high torque density and high backdrivability," pp. 1–12.

[15] J. W. Sensinger, "Efficiency of High-Sensitivity Gear Trains, Such as Cycloid Drives," *Journal of Mechanical Design*, vol. 135, no. 7, p. 071006, 2013.

[16] J. W. Sensinger and J. H. Lipsey, "Cycloid vs. Harmonic Drives for use in High Ratio, Single Stage Robotic Transmissions," *2012 IEEE International Conference on Robotics and Automation*, vol. 1, pp. 4130–4135, 2012.

[17] P. L. García, S. Crispel, E. Saerens, T. Verstraten, and D. Lefeber, "Compact Gearboxes for Modern Robotics: A Review," *Frontiers in Robotics and AI*, vol. 7, p. 103, 2020.

[18] J. W. Sensinger, "Selecting Motors for Robots Using Biomimetic Trajectories: Optimum Benchmarks, Windings, and Other Considerations," *2010 IEEE International Conference on Robotics and Automation*, pp. 4175–4181, 2010.

[19] S. Rezazadeh and J. W. Hurst, "On the Optimal Selection of Motors and Transmissions for Electromechanical and Robotic Systems," *2014 IEEE/RSJ International Conference on Intelligent Robots and Systems*, pp. 4605–4611, 2014.

[20] A. Calanca, S. Toxiri, D. Costanzi, E. Sartori, R. Vicario, T. Poliero, C. D. Natali, D. G. Caldwell, P. Fiorini, and J. Ortiz, "Actuation Selection for Assistive Exoskeletons: Matching Capabilities to Task Requirements," *IEEE Transactions on Neural Systems and Rehabilitation Engineering*, vol. 28, no. 9, pp. 2053–2062, 2020.

[21] S. J. Olney and C. Richards, "Hemiparetic gait following stroke. Part I: Characteristics," *Gait & Posture*, vol. 4, no. 2, pp. 136–148, 1996.

[22] G. Orekhov, Y. Fang, C. F. Cuddeback, and Z. F. Lerner, "Usability and performance validation of an ultra-lightweight and versatile untethered robotic ankle exoskeleton," *Journal of NeuroEngineering and Rehabilitation*, vol. 18, no. 1, p. 163, 2021.

[23] S. Zhao, K. Walters, J. M. Pérez, and R. D. Gregg, "Design and Validation of a Modular, Backdrivable Ankle Exoskeleton," *2024 10th IEEE RAS/EMBS International Conference for Biomedical Robotics and Biomechatronics (BioRob)*, vol. 00, pp. 1454–1460, 2024.

[24] S. Malhotra and M. Parameswaran, "Analysis of a cycloid speed reducer," *Mechanism and Machine Theory*, vol. 18, no. 6, pp. 491–499, 1983.

[25] F. Magnussen and C. Sadarangani, "Winding Factors and Joule Losses of Permanent Magnet Machines with Concentrated Windings," *IEEE International Electric Machines and Drives Conference, 2003. IEMDC'03*, vol. 1, pp. 333–339, 2003.

[26] D. C. Hanselman, *Brushless Permanent-Magnet Motor Design*. McGraw-Hill, 1994.

[27] H. L. Bartlett, B. E. Lawson, and M. Goldfarb, "Optimal Transmission Ratio Selection for Electric Motor Driven Actuators With Known Output Torque and Motion Trajectories," *Journal of Dynamic Systems, Measurement, and Control*, vol. 139, no. 10, p. 101013, 2017.

[28] U. H. Lee, T. Shepherd, S. Kim, A. De, H. Su, R. Gregg, L. Mooney, and E. Rouse, "How to Model Brushless Electric Motors for the Design of Lightweight Robotic Systems," *arXiv*, 2023.

[29] S. K. Au and H. Herr, "Powered Ankle-Foot Prosthesis for the Improvement of Amputee Walking Economy," Ph.D. dissertation, Massachusetts Institute of Technology, 2007.

[30] R. W. Nuckols, S. Lee, K. Swaminathan, D. Orzel, R. D. Howe, and C. J. Walsh, "Individualization of exosuit assistance based on measured muscle dynamics during versatile walking," *Science Robotics*, vol. 6, no. 60, p. eabj1362, 2021.

[31] L. H. Sloot, L. M. Baker, J. Bae, F. Porciuncula, B. F. Clément, C. Siviy, R. W. Nuckols, T. Baker, R. Sloutsky, D. K. Choe, K. O'Donnell, T. D. Ellis, L. N. Awad, and C. J. Walsh, "Effects of a soft robotic exosuit on the quality and speed of overground walking depends on walking ability after stroke," *Journal of NeuroEngineering and Rehabilitation*, vol. 20, no. 1, p. 113, 2023.

[32] Hof and L. At, "Scaling and Normalization," in *Handbook of Human Motion*, B. Müller and S. I. Wolf, Eds. Springer International Publishing AG, 2018, pp. 295–305.

[33] S. V. Sarkisian, K. Pruyn, B. M. Ortolano, R. Murray, L. Gabert, and T. Lenzi, "A Lightweight, Fully Integrated Ankle Exoskeleton With High-Torque Density Series-Elastic Actuation," *IEEE Transactions on Medical Robotics and Bionics*, vol. PP, no. 99, pp. 1–1, 2025.

[34] F. Roos, H. Johansson, and J. Wikander, "Optimal selection of motor and gearhead in mechatronic applications," *Mechatronics*, vol. 16, no. 1, pp. 63–72, 2006.

[35] M. Cooper, S. Canete, A. Eckert-Erdheim, A. Kimberley, C. Siviy, T. Baker, T. D. Ellis, P. Slade, and C. J. Walsh, "Design & Systematic Evaluation of Power Transmission Efficiency of an Ankle Exoskeleton for Walking Post-Stroke," *2024 IEEE International Conference on Robotics and Automation (ICRA)*, vol. 00, pp. 5526–5532, 2024.

`mcooper.png`

Myles Cooper In this paragraph you can place your educational, professional background and research and other interests.

`scanete.png`

Santiago Canete In this paragraph you can place your educational, professional background and research and other interests.

`dchappell.png`

Digby Chappell In this paragraph you can place your educational, professional background and research and other interests.

`cwalsh.png`

Conor Walsh In this paragraph you can place your educational, professional background and research and other interests.